

# Ballistic-aggregated Carbon Nanofoam in Target-side of Pulsed Laser Deposition for Energy Storage Applications

Subrata Ghosh<sup>1\*</sup>, Massimiliano Righi<sup>1</sup>, Andrea Macrelli<sup>1</sup>, Davide Orecchia<sup>1</sup>, Alessandro Maffini<sup>1</sup>, Francesco Goto<sup>2</sup>, Gianlorenzo Bussetti<sup>2</sup>, David Dellasega<sup>1</sup>, Valeria Russo<sup>1</sup>, Andrea Li Bassi<sup>1</sup>, Carlo S. Casari<sup>1\*</sup>

<sup>1</sup> *Micro and Nanostructured Materials Laboratory – NanoLab, Department of Energy, Politecnico di Milano, via Ponzio 34/3, Milano, 20133, Italy*

<sup>2</sup> *Solid Liquid Interface Nano-Microscopy and Spectroscopy (SoLINano- $\Sigma$ ) lab, Department of Physics, Politecnico di Milano, Piazza Leonardo da Vinci 32, 20133 Milano, Italy*

**Abstract:** In pulsed laser deposition, along conventional deposition on frontside of plasma-plume, target is getting coated on its surface too. For reproducibility, cleaning those residues is the most adopted approach. Herein, we investigate the target-side coated materials and employ them as a binder-free supercapacitor electrode. Ballistic aggregated target-side nanofoam is compact and contains higher  $sp^2$ -carbon, higher nitrogen content with higher graphitic-N and lower oxygen content with lower COOH group than that of diffusive aggregated conventional nanofoams. They are highly hydrogenated graphite-like amorphous carbon and superhydrophilic. The symmetric microsupercapacitor delivers higher volumetric capacitance of 522 mF/cm<sup>3</sup> at 100 mV/s and 104% retention after 10000 charge-discharge cycles over conventional nanofoam (215 mF/cm<sup>3</sup> and 85% retention) with the areal capacitance of 134  $\mu$ F/cm<sup>2</sup> at 120 Hz and ultrafast frequency response. Utilizing those residue materials is of great importance towards sustainable development, zero-waste, and utilization of deposition techniques in full-phase, which is resource-efficient, energy competent and cost-effective.

*Keywords: Pulsed Laser Deposition, nanocarbons, Plasma plume, micro-supercapacitor, Energy storage*

Corresponding author email: [subrata.ghosh@polimi.it](mailto:subrata.ghosh@polimi.it) (S.G.) and [carlo.casari@polimi.it](mailto:carlo.casari@polimi.it) (C.S.C.)

## Introduction

Cultivating nanomaterial thin films with adequate morphology and properties has received tremendous attention from the community for their potential application since the beginning.[1],[2][3] The development of various deposition techniques and their advances are direct consequences. Among the widely used techniques, Pulsed Laser Deposition (PLD) has established its ground for preparing materials from carbon to metal oxides, from compact film to 3D porous structures, heterostructures to layered structures and so on.[4],[5],[6] It must be noted that the substrates, on which the desired film is to be grown, are generally placed in front of the target material such that the ablated species with high kinetic energy travel forward and get deposited on the substrate (Figure S1a).[7] During the synthesis process at high deposition pressure under background gas(es), once the laser is irradiated with a certain fluence (energy per pulse per unit area), some ablated species are redeposited on the target too (Figure 1b). The species formed inside the plasma plumes are mostly excited atoms, dimers etc, which are responsible for growing the materials on the substrate. Indeed, in the case of laser ablation of a carbon target, it has been reported that  $sp$ -hybridized carbon atomic wires have been observed on the vicinity of highly oriented pyrolytic graphite (HOPG,  $sp^2$ -hybridized) target itself.[8] For the reproducibility of the desired conventional materials, the traditional approach is cleaning out the residue or scrap materials from the target after every single synthesis process by either laser cleaning and/or chemical cleaning. However, there is rare investigation on allowing the backward ablated species to obtain nanostructured films on a substrate placed at the target side. The above-mentioned background makes us pose the arising questions and effort to clear up them in this dedicated investigation: how those backward ablated species form a structure if a substrate is provided, how the morphology and properties will be and how they differ from the conventional materials grown in PLD and is there any possibility to be used in potential applications.

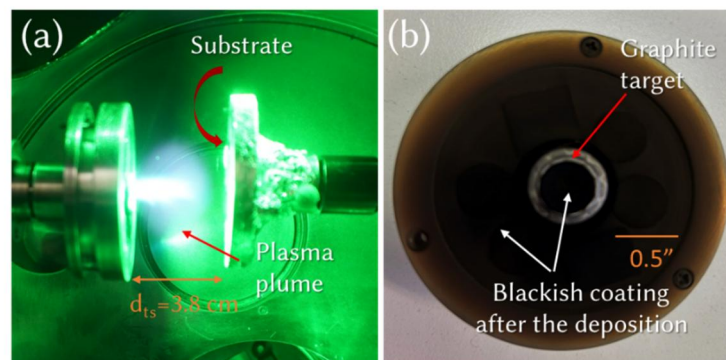


**Figure 1:** Optical micrograph of (a) plasma plume during the deposition of nanostructures by pulsed laser deposition with 532 nm laser and (b) target holder after the deposition with the blackish coating. Here, the substrate is placed on the rotating substrate holder in front of the plasma plume and the target is also rotated without any translational motion.

In this respect, carbon-based materials are quite popular as supercapacitors or electrochemical capacitors, where supercapacitors have higher energy density than conventional capacitors and higher power density than conventional batteries. Nowadays, microsupercapacitor or thin film-based supercapacitors have received significant attention as portable, wearable, lightweight and miniaturized energy storage devices and *a.c.* line filtering applications.[9],[10] However, for carbon-based materials, the major drawbacks are the hydrophobicity in aqueous media,[11] limited density of states,[12] and ten-to-hundred times lower specific capacitance than that of pseudocapacitive materials[13]. On over it, to fabricate the electrode, most of the carbon-based materials are mixed with a conducting agent and binder, which limits the conducting pathways for the electrolyte ions,

cycle stability and sometimes the electrode materials become resistive. This fact also limits the ability to operate at relatively low working frequencies (below 1Hz). Thus, the design of binder-free, conducting agent-free, and self-standing suitable electrode materials for high-frequency microsupercapacitor applications is necessary. With this motivation, we placed the graphite target on a target holder with large diameter, and the empty spaces in the holder crown were filled with substrates (Figure S1a-b). Carbon nanofoam at target-side (CF-T) was synthesized at room temperature by PLD and conventional one (CF-C) is deposited in same growth run (Figure S1c-d). A thorough structural and morphological investigation and utilization as supercapacitor electrode with excellent cycle stability and ultrafast frequency response were carried out for the first time to the best of our knowledge.

## EXPERIMENTAL SECTION

**Synthesis of carbon nanofoam.** Carbon nanofoam was deposited on the target side (CF-T) by placing the substrates, Si and carbon paper, on the 2-inch target holder around the 0.5-inch graphite target. The pressure of the deposition unit was maintained at 300 Pa under N<sub>2</sub>-H<sub>2</sub> (95%-5%) environment and the ablation was performed using a Nd:YAG pulsed ns-laser (2<sup>nd</sup> harmonic at 532 nm, pulse duration 5-7 ns, repetition rate 10 Hz) for 15 min with a pulse energy of 420 mJ and fluence of 6.5 J/cm<sup>2</sup>. For the conventional deposition, bare carbon nanofoam (CF-C) was deposited on substrates in front of the target at a defined distance of 3.8 cm from graphite. Both the target and substrate holder were rotated to uniformly ablate the species and deposit on the substrate, respectively. Prior to the deposition, the chamber was evacuated down to 10<sup>-3</sup> Pa. Optical micrographs of substrate placed on the target side and substrate sides before and after deposition are given in Figure S1.

**Microscopy.** The morphology of obtained materials was acquired using a field-emission scanning electron microscope (FESEM, ZEISS SUPRA 40, Jena, Germany) and inLens detector operated in a high vacuum. Electron Dispersive spectra (EDS) were recorded at the acceleration voltage of 20 kV using Aztec software to evaluate the elemental analysis and the instrument is equipped with a Peltier-cooled silicon drift detector (Oxford Instruments). To calculate the mass density of the film, a MATLAB code called EDDIE software was used. With the input of average height information of the material and the details of substrate reference (Si for our case), one can estimate the mass density of the film using the data obtained from EDS analysis.

Considering the density of graphite ( $\rho_{graphite}$ ) of 2.2 g/cm<sup>3</sup> and using the mass density estimated from EDDIE software, the porosity of the grown material is calculated using the formula of % porosity =  $(1 - \rho_{ACF} / \rho_{graphite}) \times 100$ .

### Spectroscopy.

The XPS data were acquired using a non-monochromatized x-ray source using a Mg anode (photon energy 1253.6 eV), maintained at a power of 200W. The kinetic energy of the photoemitted electrons was measured using a hemispherical analyzer with a 150mm mean radius, PHOIBOS150 from SPECS GmbH. The spectra were acquired with a pass energy of 20 eV, with an energy resolution of 0.9 eV (FWHM). The pressure in the measurement chamber during the experiments is about 1x10<sup>-10</sup> Torr. Peaks were fitted after Shirley background subtraction using CasaXPS software, and at.% of elemental compositions were extracted from peak area ratios after correction by Scofield relative sensitivity factors (C = 1.0, N = 1.77, O = 2.85).[14] For C1s, the asymmetric *sp*<sup>2</sup>-C peak is fitted with Gaussian-Lorentzian lineshape (GL(30)) with asymmetric factor (T200)[15] and other symmetric carbon peaks with GL(30) by setting the range of full width at half maximum to 1.2–2 eV. The FWHM of oxygenated carbon peaks, deconvoluted O1s peaks, and deconvoluted N1s peaks are set to 1.8-2.2

eV.[16] The  $sp^3$ -C peak is generally shifted by 0.7-1 eV from  $sp^2$ -C and hydroxyl/ether, carbonyl and carboxylic groups are shifted approximately 1.5, 3, and 4.5 eV higher, respectively.[16]

The Raman spectra of all samples were collected using a Renishaw Invia Raman spectrometer, UK. A 514 nm laser with a power of 0.04 mW, a 1800 gratings spectrometer and a 50X objective lens were used to collect the spectra, with accumulation time of 5 s. The background correction of each spectrum is carried out using the WIRE software, provided by the instrument, using polynomial baseline fit with 5<sup>th</sup> order and normalized. The Raman spectra of grown materials were deconvoluted using MATLAB. The D-peak was fitted with a Lorentzian line-shape and the G-peak with a Breit-Weigner-Fano line-shape. The fitted spectra are supplied in the Supporting Information.

**Electrochemical measurements.** The electrochemical performances of the samples were carried out in 2-electrode configuration using Swagelok Cell (SKU: ANR-B01, Singapore). and 6M KOH used as an electrolyte. The hydrophobic PP membrane is modified by a two-step process: soaked with acetone at 20 °C for 5 min and followed by aqueous 6M KOH solution at 20 C, and used after 1 hr.[17] The cell was assembled by sandwiching separator-soaked-electrolytes between the carbon foam electrodes grown on carbon paper. For the electrochemical testing, carbon foams and modified separator were dipped into the electrolyte solution for 1hr. Cyclic voltammogram, charge-discharge test and electrochemical impedance spectra were recorded using a PALMSENS electrochemical workstation. The cyclic voltammetry at different scan rates ranging from 20 to 1000 mV/s and charge-discharge at different current densities of 150 to 500  $\mu$ A were carried out and scanned within the defined voltage at 100 mV/s for 1000 times. The areal capacitance is calculated using the equation:

$C_{areal} = \int I dV / A.v. \Delta V$ , where  $I$  is the current,  $v$  is the scan rate,  $A$  is the geometric area of the electrode and  $\Delta V$  is the voltage of the device. Single electrode capacitance = 4  $\times$  device capacitance. The volumetric capacitance of electrode materials is estimated by dividing the areal capacitance by the total height of two carbon nanofoam electrodes. The electrochemical impedance spectroscopy is conducted in the frequency range of 1 Hz to 0.1 MHz at open circuit potential with a 10 mV *a.c.* perturbation. The energy density ( $E_A$ ) of the device is calculated via the equation:  $E_A = C_{dl}V^2/2$ , where  $C_{dl}$  is the double layer capacitance at 120 Hz obtained from the areal capacitance versus frequency plot. The relaxation time constant is calculated from the impedance spectra at 120 Hz using the equation:  $\tau_{RC} = -Z'/2\pi fZ''$ , where  $Z'$  and  $Z''$  are the real and imaginary components of impedance.

## Results and Discussion

Carbon nanofoams on target-side and substrate-side are synthesized using pulsed laser deposition at room temperature. The synthesis procedure is detailed in the experimental section. [Figure 2](#) displays the field-emission scanning electron micrographs of the target-side nanofoam (CF-T) grown on Si. Similar morphological characteristics for the sample grown on carbon paper are observed ([Figure S2a](#)) and used for supercapacitor test. The tree-like CF-T have an average height of 8.6  $\mu$ m ([Figure 2b-c](#)) and they are quite packed with a porosity of 79%. The mass density of CF-T is estimated to be 0.45 g/cm<sup>3</sup> (EDDIE software,[18] fitted spectra are provided in [Figure S2d](#)). Moreover, the binder-free nanofoam surfaces are found to be superhydrophilic, which facilitates efficient electrolyte ion adsorption and desorption, effective ion transportation, and ion transfer kinetics upon its utilization as active energy storage electrode (inset of [Figure 2b](#)). Based on the electron micrographs ([Figure 2c and 2g](#)), a good conformal growth capability that is necessary for substrates with complex geometry is evidenced. The summary of morphology and vertical height of the sample is presented in [Figure S2\(b\)](#). The chemical compositions, as confirmed by EDS ([Figure 2d](#)) and XPS ([Figure 3a](#)), are found to be carbon as a primary element, bulk- and surface-functionalized nitrogen (as N<sub>2</sub>-H<sub>2</sub> was used as background gas in deposition), and surface-functionalized oxygen. In contrast, CF-C, with an average

vertical height (20  $\mu\text{m}$ ) is found to be taller compared to the CF-T, more porous (porosity  $\sim 93\%$ ) and lighter (mass density  $\sim 0.14 \text{ g/cm}^3$ ). Surprisingly, no signature from nitrogen is found for the CF-C from EDX measurement.

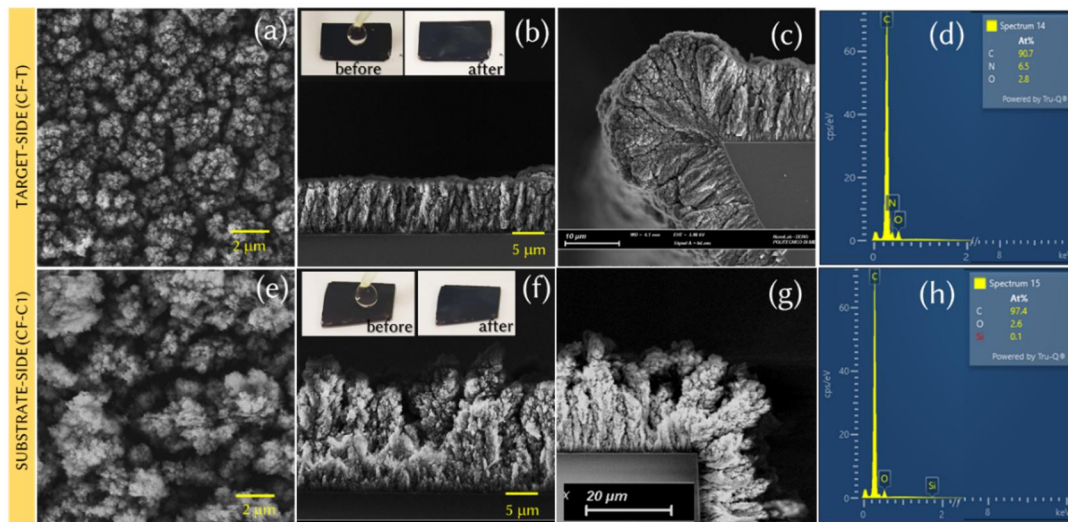


**Figure 2:** (a) Top-view and (b-c) cross-sectional view and (d) EDX spectra with elemental quantification of CF-T. (e) Top-view and (f-g) cross-sectional view and (h) EDX spectra with elemental quantification of CF-C. The inset of Figures 2(b) and 2(f) are the photographic images of the water droplets on CF-T and CF-C, respectively, where volume of water droplet was 10  $\mu\text{l}$ .

The XPS survey spectra of studied samples are shown in Figure 3a, the variation in the sample found is an atomic concentration of oxygen and nitrogen while carbon concentration is almost the same (table in inset of Figure 3a). The presence of oxygen and nitrogen functionalities not only known to improves the wettability of the carbon materials but also contributes to the quantum capacitance and pseudocapitance while employing the material as an energy storage electrode.[12] The elemental analysis confirmed the presence of 10 at% of nitrogen in the CF-T, which is higher than that of CF-C (6.4 at%). The higher amount of nitrogen content in CF-T is due to the higher reactivity of nitrogen inside the plasma plume (more radicals etc.). In the plasma plume, there is also a possibility of nitrogen ions formation and deposition on the target-side, where the path is short, and they cannot be stopped by collision with the background gas. They could be instead mainly stopped on the substrate-side, recombining into  $\text{N}_2$  without significant film incorporation. The fact that on substrate-side we can see nitrogen with surface-sensitive XPS and not with EDS can be somewhat related to this: in substrate-side the nitrogen could be just surface contaminants. On the other hand, CF-C contains relatively higher atomic oxygen concentration (30.9%) than that of CF-T (26.4%), which is due to the higher porosity of CF-C.

The full width at half maximum (FWHM) of the  $\text{C}1\text{s}$  peak of CF is found to be around 2.2 eV (Figure 3b), which is much higher than that of highly oriented pyrolytic graphite (HOPG) (0.8 eV). The broadened  $\text{C}1\text{s}$  peak indicates the CF is amorphous in nature, which is investigated further by Raman spectroscopy and discussed later. The best fit for high-resolution  $\text{C}1\text{s}$  for our carbon film is obtained by introducing the additional peak observed at around 283.8 eV along with  $\text{sp}^2\text{-C}$  ( $\sim 284.8 \text{ eV}$ ),  $\text{sp}^3\text{-C}$  ( $\sim 285.5 \text{ eV}$ ) and other functionalized carbon bindings (Figure 3b). The high-resolution  $\text{C}1\text{s}$  spectra can be fitted by two carbon peaks ( $\text{sp}^2\text{-C}$  and  $\text{sp}^3\text{-C}$ ) and functionalized carbon peaks. However, the fitting with those deconvoluted peaks leads to higher residual standard deviation at lower energy (see Figure S3). For the carbon nanostructures formed by plasma-assisted growth, the peak at lower binding energy ( $\sim 283.8 \text{ eV}$ ) is assigned as the vacancy defect.[19] Even, the peak at lower binding energy has been reported for the defected HOPG, prepared by sputtering with 60 eV  $\text{Ar}^+$  ions.

Supported by density-functional theory calculations, a chemical shift towards a lower binding energy for the all carbon atoms surrounding a single vacancy in hexagon matrix has been reported with respect to the C1s peak of a perfect HOPG (284.5 eV).[20] In the case of amorphous CF grown at more than 30 Pa under Ar gas, onion-like-carbon is found to be embedded in the CF matrix from the transmission electron micrograph.[21] The presence of onion-like-carbon indicates the existence of heptagon-pentagon structure in the CF matrix.[21] This peak is also assigned as defected graphitic peak for the amorphous carbon thin film prepared by ion-beam sputtering technique.[22] Moreover, the peak at around 283.8 ( $\pm 0.3$ ) eV obtained after deconvoluting C1s peak of carbyne-like carbon films[23], nanothick amorphous carbon[24], and nanostructured carbon materials is assigned to the  $sp$ -C.[25] In our case, as CF is prepared at room temperature by laser sputtering the graphite in PLD, we observed  $sp$ -carbon in agreement with our previous work.[26] The fitting of the  $sp$ -C along with the  $sp^2$ -C and  $sp^3$ -C is also reported for the  $sp$ -bonded carbon chains on the graphite surface prepared by femtosecond PLD[8] and the amorphous carbon[25]. It has been reported[25] that  $sp$ -C content in amorphous carbon decreases when it is annealed. Therefore, the peak at 283.8 eV is attributed to the  $sp$ -C and/or vacancy defect present in our CF. To validate the  $sp$ -C presence in the structure, the Raman spectra were collected for longer accumulations, which is discussed later. Indeed, more investigation on  $sp$ -C binding energy and its contribution to total C1s are the subject of further experimental and theoretical investigations, which is not the focus of this current research. Among the samples, CF-T shows relatively higher  $sp^2$ -C and lower  $sp^3$ -C content than that of CF-Cs (Figure 3c), which could have impact on the electrochemical performances.

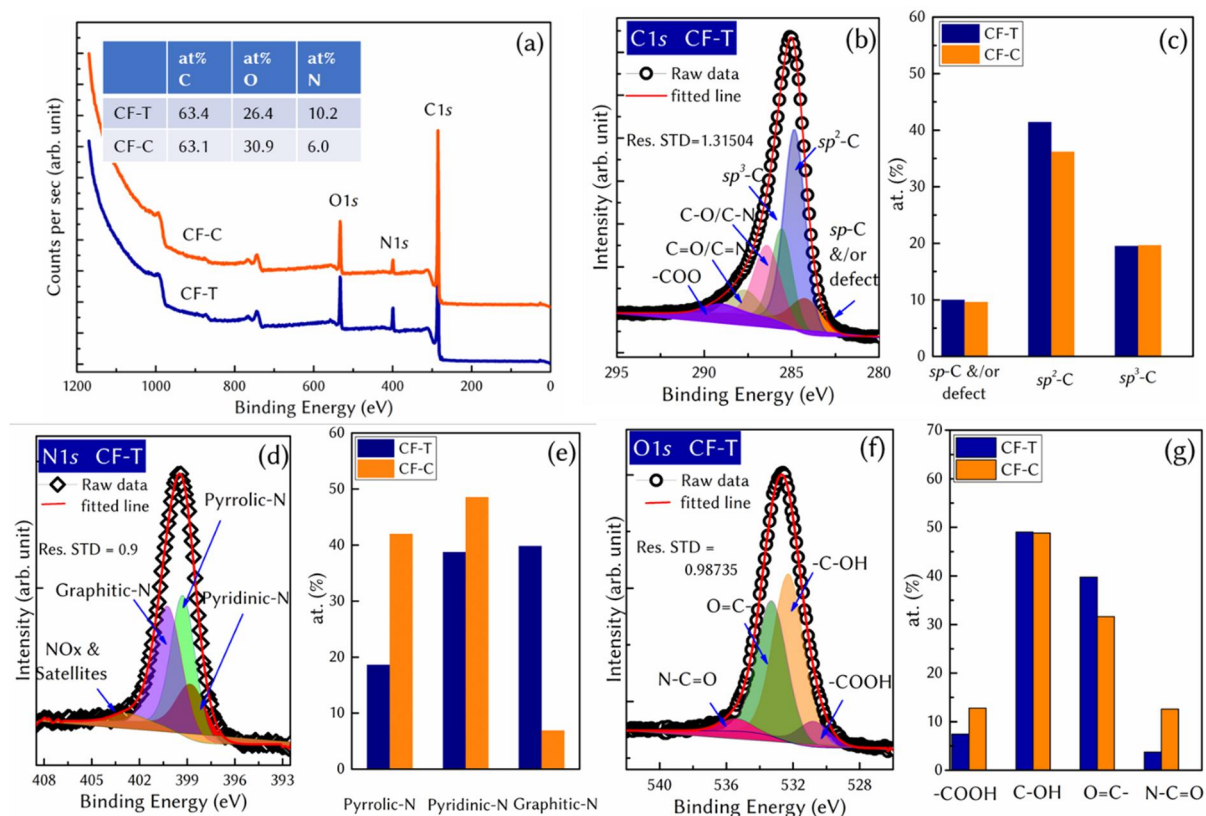


**Figure 3:** (a) Survey scans with at. % of C, O and N of CF-T and CF-C at inset. High resolution (c) C1s spectra with (d) relative contribution of carbon components. (e) High-resolution N1s with (f) relative at. % concentration of individual functional groups, and (g) High-resolution O1s spectra with (h) relative at. % concentration of individual functional groups of CF-T and CF-C.

The high-resolution N1s spectra of CF-T (Figure 3d) is deconvoluted into four peaks: pyridinic-N, pyrrolic-N, graphitic-N and NO<sub>x</sub> or satellite peaks. From the analysis, the graphitic N-content at 400.2 eV in CF-T sample is found to be higher than that of CF-Cs (Figure 3e). On the other hand, CF-C has the highest content of pyridinic-N at 399.2 eV and pyrrolic-N at 399.9 eV. It can be also seen from the high-resolution O1s spectra (Figure 3f) that the different CF samples have different content of oxygen functional groups on the surface as they have grown at different distances and zone in the plasma plume. From Figure 3g, it is clear that the CF-C contains a higher amount of -COOH groups compared to the CF-T. The -COOH group is mostly unstable and leads to poor cycle stability of electrodes for longer charge-discharge cycles.[27] The high-resolution spectra of N1s and O1s for CF-C with deconvoluted peaks are provided in Figure S4.

The Raman spectra of both CFs (Figure 4a) consist of a large band related to the *sp*<sup>2</sup> signal, composed by two components, namely D peak at around 1368 cm<sup>-1</sup> and G-peak at about 1576 cm<sup>-1</sup>, along with very a weak *sp*-band (inset of Figure 4a) and a small, modulated bump in the region of 2400-3200 cm<sup>-1</sup>. A similar feature in the Raman spectra samples grown on carbon paper is noticed (Figure S5). The weak *sp*-C feature obtained in Raman spectra[26] is in agreement with the very low *sp* content extracted from XPS data. Figure 4a also indicates the presence of photoluminescence background, which is usually related to the existence of hydrogen in the sample.[28] It is noteworthy to mention that CF-T has higher photoluminescence than that of CF-C. To estimate the hydrogen-content in the sample from these spectra, we tentatively use the formula reported in Ref. [28], which investigated a broad range of hydrogenated amorphous carbon (*a*-C:H) material. The quantitative formula used is  $H [at. \%] = 21.7 + 16.6 \log \left[ \frac{m}{I_G} (\mu m) \right]$ [28], where *m* is the slope of first order Raman spectra within the region of 900 to 1900 cm<sup>-1</sup> (Figure 4b) and *I<sub>G</sub>* is the intensity of the G peak (calculated from the G-peak fitting with Breit-Weigner-Fano line-shape, Figure S5). The photoluminescence background ( $\frac{m}{I_G}$ ) for CF-T and CF-C found to be 4.32 and 3.58 μm, respectively, not so far from the typical value of highly-hydrogenated graphite-like amorphous carbon (GLCHH) which is reported to be around 5 μm.[28] The higher the slope and/or ratio of  $\frac{m}{I_G}$ , the more hydrogenated the sample is. This fact suggests that CF-T is more hydrogenated than CF-C and this would agree with the fact that on the target side most reactive species are available. The estimated hydrogen content of CF-T and CF-C, using the above-mentioned formula, are 32.2% and 30.9%, respectively. On the other hand, XPS analysis reminds us that both the CFs contain around 19% *sp*<sup>3</sup>-C (C-C *sp*<sup>3</sup>+ C-H *sp*<sup>3</sup>). Moreover, to derive the type of hydrogenated carbon from Raman spectra one needs to pay attention also to the G-peak position and the *I<sub>D</sub>/I<sub>G</sub>* intensity ratio plotted with respect to estimated hydrogen content, as reported in Ref.[28] and adapted in Figure 4c. Using our data, we realize that our CFs do not fall into the extrapolated line of *a*-C:H (red line in Figure 4c) of Ref. [28]. This is an indication that the presence of nitrogen in CFs, while not giving any contribution to photoluminescence, influences the Raman signal, namely the D and G peaks. Actually, it is known that nitrogen has a significant role, in clustering and bonding environment of different hybridized carbon.[29] We tentatively use the three-stage model for amorphous carbon nitride containing hydrogen reported in Ref. [29] and adapted in Figure 4d. Plotting the G-peak position and *I<sub>D</sub>/I<sub>G</sub>* of our samples with respect to the *sp*<sup>3</sup>-C content (obtained from XPS: 19.51% for CF-T and 19.66% for CF-C), it appears that our CFs falls in the nonuniqueness region of stage II of the model. Actually, N<sub>2</sub>-H<sub>2</sub> background gas is used for the deposition and the presence of nitrogen content in the CF (~10 at. % in CF-T and 6% at. % in CF-C) is confirmed from XPS.

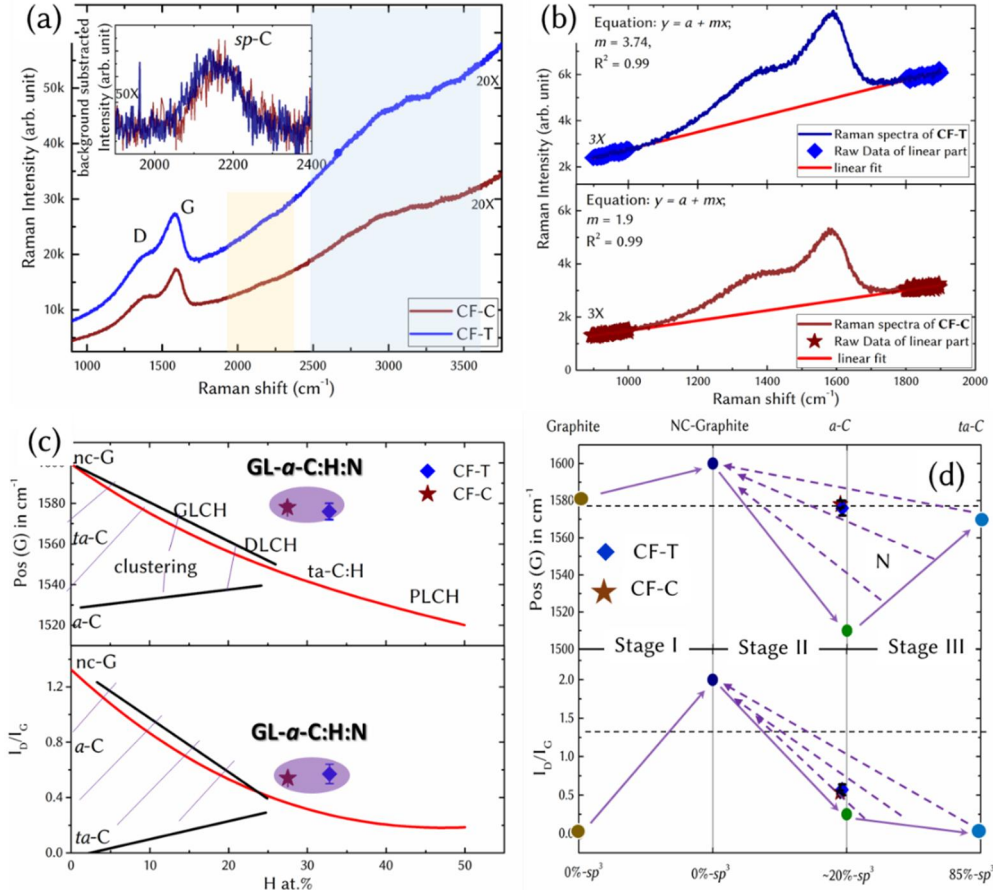


**Figure 4:** (Color online) Raman spectra of CF-T with the laser used of 514 nm with photoluminescence background. (b) First-order Raman spectra of CF-T at top and CF-C at bottom with the linear fit of Raman data of linear regions in the range of 900 to 1900  $\text{cm}^{-1}$  ( $\blacklozenge$  and  $\star$  in the graph belongs to CF-T and CF-C, respectively). Plot of G-peak position and  $I_D/I_G$  of carbon nanofoam (c) with respect to the hydrogen-content and (d) in Ferrari-Robertson's amorphization trajectory model. The red and black solid line in (c) is the fitted data extracted from the extrapolated fitted line from the Ref.[28] using the WebPlotDigitizer software authored by Ankit Rohatgi. Shaded regions are non-uniqueness region at low hydrogen-content. GLCH, DLCH, ta-C:H and PLCH represent graphite-like, diamond-like, tetrahedral and polymeric hydrogenated amorphous carbon (*a*-C), respectively. nc-G, ta-C and GL-a-CHHN represent nanocrystalline graphite, tetrahedral *a*-C and highly hydrogenated graphite-like *a*-C nitride. In Figure 4(d), solid lines are guided to eye to indicate the transition of one stage to another stage and the dashed arrow lines represent in nonuniqueness region due to the incorporation of nitrogen in amorphous carbon.[29]

The higher amount of heteroatoms like hydrogen, oxygen and nitrogen for CF-T is also reflected in the Raman spectra as we see broadened FWHM of D-peak ( $281.7 \pm 34.5 \text{ cm}^{-1}$ ) and G-peak ( $127.6 \pm 6.6 \text{ cm}^{-1}$ ) compared to that of CF-C ( $249.5 \pm 17.8 \text{ cm}^{-1}$  for D-peak and  $121.4 \pm 1.5 \text{ cm}^{-1}$  for G-peak). Thus, according to the classification of hydrogenated *a*-C and *a*-C:N,[28],[29] and the above analysis, the CFs prepared by PLD can be called as nitrogen-containing graphite-like *a*-C:H (GL-*a*-C:H:N). A systematic investigation on the GL-*a*-C:H:N can be the subject of further research.

The distinctively columnar morphology of CF-T films is indicative of a ballistic aggregation, in contrast with the diffusive aggregation typical of fractal-like ultra-low density nanofoams deposited at higher background pressure and lower fluence.[30] Since the ablated material is ejected with a non-zero momentum toward the substrate, one can argue that the CF-T deposits are grown by species that have undergone a back-reflection caused by single or multiple large angle collisions with background gas atoms and molecules, likely occurring in the vicinity of the ablation region. For this reason, the mean path traveled by the species that arrive on the target side can be considerably shorter than that of species landing on the substrate. In a ballistic regime, the energy lost by the



ablated species is proportional to the number of collisions with the background gas: the longer the traveled path, the lower is the kinetic energy of the species that contribute to the film growth. As a result, the morphology of the CF-T deposits is indeed less porous, containing higher hydrogen and nitrogen-content than CF-T ones, hinting to a lower kinetic energy for the conventional deposition compared to the target-side. It is worth noting that it is not straightforward to obtain the same morphology of CF-T in a conventional configuration by simply reducing the target-to-substrate distance. Indeed, such a configuration would imply that the film is grown by a mixture of very energetic species that have undergone few or no collisions and low energy species resulting from many small angle collisions. This difference certainly has an impact on their performance as an active material for desired applications.

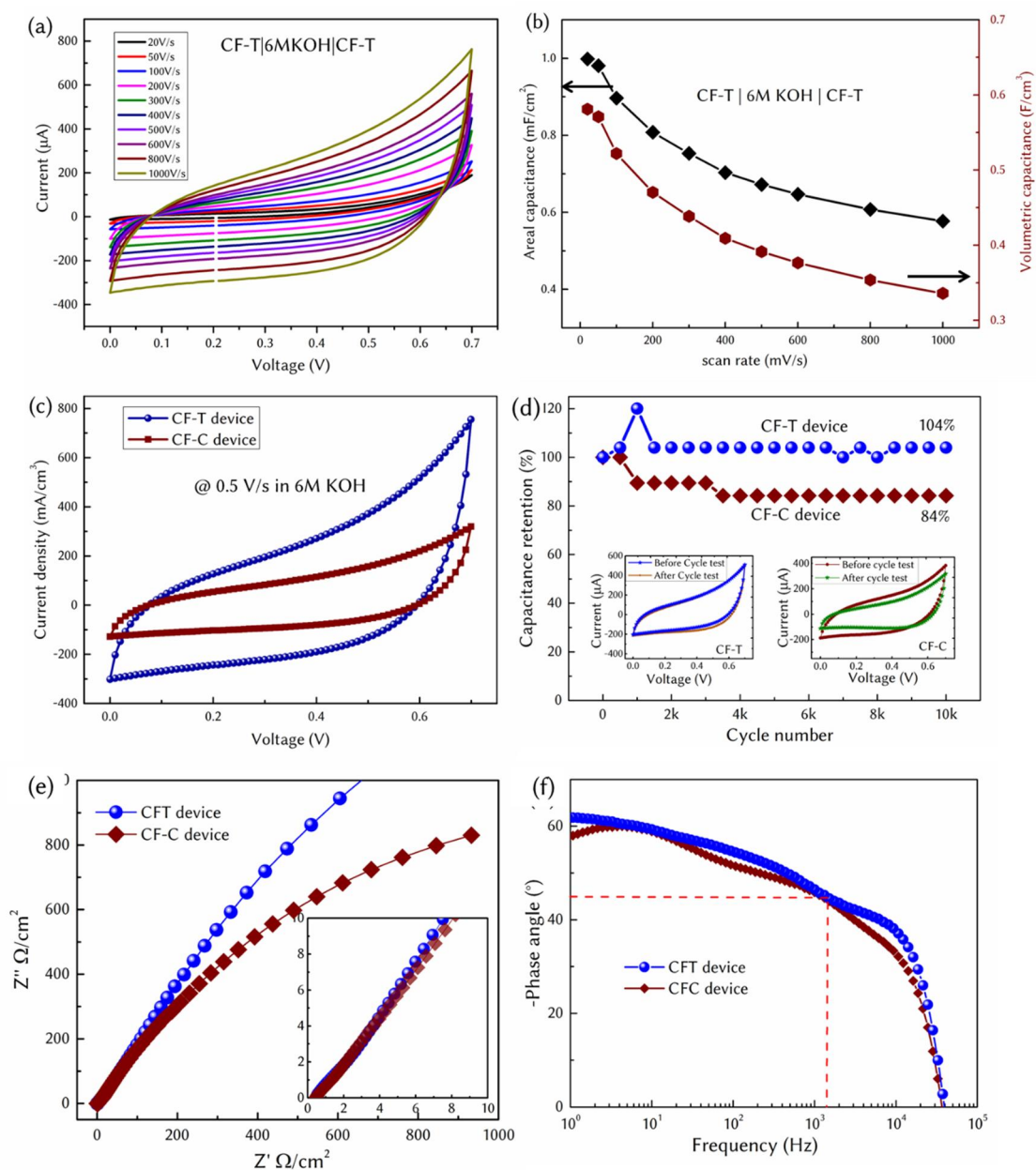


**Figure 5 (color online):** Electrochemical performances. (a) Cyclic voltammogram and (b) specific capacitance at different scan rates for the CF-T symmetric device. (c) comparative cyclic voltammogram and specific capacitance at the 0.5 V/s scan rate of CF-T and CF-C1 symmetric device. (d) cycle stability of both devices at 160  $\mu\text{A}/\text{cm}^2$  with the cyclic voltammogram profile at 0.5 V/s of each device before and after 10000 charge-discharge cycles. (e) Nyquist plot and (f) Bode plot of CF-T and CF-C device.

Figure 5(a) shows the scan rate-dependent cyclic voltammogram (CV) of CF-T symmetric microsupercapacitor device. The shape of CV is quasi-rectangular with a mirror-image feature and maintained its shape with respect to the scan rate indicating excellent capacitive behavior of the device within 0 to 0.7 V. The deviation from perfect rectangular CV shape is due to the pseudocapacitive contribution from the oxygen and nitrogen functional groups present on the surface of nanofoam. The areal/volumetric capacitance of the microdevice is estimated and plotted with respect to the scan rate in Figure 5(b). The CF-T microdevice is capable of providing higher volumetric capacitance ( $522 \text{ F/cm}^3$ ) with higher rate performance of 64% at 1 V/s compared to 0.1 V/s than that of the CF-C ( $215 \text{ F/cm}^3$ , 54% retention) (Figure 5(c-d)). The CV at different scan rate and the plot of normalized capacitance with respect to the scan rate are provided in Figure S7a-b. Moreover, CF-T microdevices deliver better cyclic stability of 104% upto 10000 charge-discharge cycles (Figure 5e) and remains unchanged CV profile in contrast to the CF-C microdevice (cycle stability ~ 85%). The outperformance of CF-T microdevice compared to the CF-C microdevice in charge-storage can be attributed to the higher  $sp^2$ -C, lower oxygen content with lower unstable COOH group[27] and higher nitrogen-content with higher graphitic-N.[31] The charge-discharge profile of CF-T and CF-C is provided in Figure S7c-d. The increased capacitance retention of 104% after 10000 charge-discharge cycles for the CF-T can be attributed to the activation process of electrode materials during the charge-discharge.

Figure 5e shows the Nyquist plot with the high-frequency zone (inset of Figure 5e) and it can be seen that the CF-T is steeper than the CF-C indicating relatively faster ion diffusion and better capacitive behaviour, which could be due to the low charge-transfer resistance and electrode resistance of CF-T. At  $-45^\circ$ , the corresponding frequency is found to be 1321.9 Hz for the CF-T, which is higher than that of CF-C (1149.75 Hz). The phase angle of CF-T and CF-C is estimated to be  $-54^\circ$  and  $-58.4^\circ$  at 120 Hz (Figure 5f). Although the phase angle of the CF at 120 Hz is lower than the ideal capacitor ( $-90^\circ$ ), it is comparable and/or better than many existing reports (Table 1). The frequency-dependent areal capacitance of CF-T device is plotted in Figure S8. At 120 Hz, areal capacitance is calculated to be  $134 \mu\text{F/cm}^2$  and corresponding areal energy density is  $32.8 \mu\text{FV}^2/\text{cm}^2$ . The relaxation time constant response time for CF-T and CF-C is found to be 0.86 and 0.76 ms, respectively. The resistor-capacitor time constant is found to be 0.12 ms for CF-T. These results indicate that the CF electrode maintains fast frequency response.

Carbon nanofoam was also synthesized using hydrothermal method[32], sol-gel method[33], pyrolysis[34], laser processing of graphene oxide[35], chemical vapor deposition,[36], etc. by other groups and used for different applications. All the carbon nanofoams prepared by the above-mentioned method either use high temperature and/or involve multi-steps to get the final structure. On over it, the signature of  $sp^2$ -C from those nanostructures is hardly seen, and they are not hydrophilic, and lightweight material as carbon foam prepared by room temperature PLD in our case. For example, carbon nanofoam synthesized at high temperature by chemical vapor deposition is hydrophobic in nature.[36] Moreover, the carbon nanofoam deposited in frontside and backside of the target ensures the possibility of growing carbon nanofoam with different characteristics in single production run at room temperature. The room temperature growth offers to grow the nanostructure on any flexible substrate. To show the versatility of our approach, we demonstrate porous nanostructures (on the substrate placed at the front-side of plasma plume), compact (on the substrate placed within the target of target-side), and intermediate nanostructure (on the substrate placed outside the target in target-side) by ablating the species from both targets simultaneously by illuminating with a single laser in one synthesis process (Figure S9).

**Table 1:** Comparison of microsupercapacitor devices with frequency response (\* represents the calculated value using the data available in the cited reference)

Electrode materials	Electrolyte	Areal capacitance (CV or CD) in mF/cm <sup>2</sup>	Areal capacitance at 120 Hz (EIS) (μF/cm <sup>2</sup> )	Areal energy density (μFV <sup>2</sup> /cm <sup>2</sup> )	Phase angle at 120 Hz (°)	Frequency (Hz) / Relaxation time constant (ms) at -45°	Resistor-capacitor time constant (ms)	Cyclic stability
CF-T, thickness ~8.6 μm	6M KOH	0.9 at 100 mV/s	134	32.8	-54.04	1321.9/0.86	0.12	104% after 10 <sup>5</sup> cycles at 125 μA
CF-C, thickness ~20 μm		0.87 at 100 mV/s	127	31.1	-58.39	1149.75/0.76	0.14	84% after 10 <sup>5</sup> cycles 125 μA
O-PGF[37]	0.1 M LiClO <sub>4</sub>	3.8 at 25 μA/cm <sup>2</sup>	755	377.5*	-53	- / 1.46	0.98	96.7% after 500 μA/cm <sup>2</sup>
EOG/CNF, thickness ~1 μm[38]	6M KOH	-	370	149.85*	-81.5	22000 / 0.07	-	98% after 10 <sup>6</sup> cycles at 40 mA/cm <sup>2</sup>
	1 M TEABF <sub>4</sub> /AN	-	160	-	-80	8500 / 0.12	-	-
LCTH[39]	EMIMBF <sub>4</sub> ionic liquid	-	118	721*	-61.5	1121.3 / 0.89	0.7	101% at 14000 cycles at 10 V/s
VOG[40]	25% KOH	-	87	43.75*	-82	15000 / 0.067	0.2	-
CNT[41]	0.5 H <sub>2</sub> SO <sub>4</sub>	-	601	192*	-81	- / 0.702	0.199	-
CNT[42]	EMImNTf <sub>2</sub>	-	128	576*	-80.1	- / 0.794	-	-
EPDC[43]	1 m TEABF <sub>4</sub>	-	225	703.25	-76.5	- / 0.8	0.46	97.5% after 5000 cycles at 25 μA
pristine carbon[44]	1 M TEABF <sub>4</sub> in AN	-	444	-	-80	890/1.2	-	-
N-doped carbon[44]		-	545	-	-67	280/0.56	-	-
P/N-doped carbon[44]		-	30	-	-82	13200 / 0.077	-	-
B/N-doped carbon[44]		-	99	-	-83	5200 / 0.2	0.13	-

(CV: cyclic voltammogram, CD: charge-discharge, O-PGF: 3D ordered porous graphene, EOG: edge-oriented graphene, CNF: carbon nanofiber, LCTH: laser-processed carbon-Titanium carbide heterostructure, VOG: vertically oriented graphene, CNT: carbon nanotube, EPDC: Electrospun Polymer-Derived Carbyne, TEABF<sub>4</sub>: Tetraethylammonium tetrafluoroborate, AN: acetonitrile, EMIMBF<sub>4</sub>: -Ethyl-3-methylimidazolium tetrafluoroborate, EMImNTf<sub>2</sub>: 1-Ethyl-3-methylimidazolium bis(trifluoromethane sulfonyl)imide)

## Conclusion:

In conclusion, the carbon nanofoam on the target-side (CF-T) is successfully grown using pulsed laser deposition along with the conventional CF (CF-C) at room temperature in a single production run. The morphology and structural properties of CF-T are found to be different in terms of porosity, mass density, height, and degree of graphitization than the CF-C, which is attributed to the different aggregation under complex plasma species' behaviour in forward (diffusive aggregation) and backward (ballistic aggregation) directions. CFs is found to be highly hydrogenated nitrogen-containing graphite-like amorphous carbon and superhydrophilic. The CF-T (CF-C) microsupercapacitor delivered a high areal capacitance of 0.9 (0.87) mF/cm<sup>2</sup> and volumetric capacitance of 521 (215) mF/cm<sup>3</sup>, maintained 104% (84%) capacitance retention after 10000 after charge-discharge cycles, and showed excellent frequency response with the capability of fast charge delivery. The better performance of uniquely obtained CF-T compared to conventional CF-C is attributed to the compactness, and higher *sp*<sup>2</sup>-carbon content, higher content of N-functionalities

over O-functionalities, higher graphitic-N, and lower COOH. It can be concluded that the proposed strategy of obtaining more than one nanostructure from single deposition without additional resource, effort, and time, is versatile, of significant value for large-scale production, sustainable, and offers to achieve a net zero waste goal. The binder-free self-supporting active materials can be used for flexible optoelectronics, micro energy storage device and other desired applications. . This easily adaptable strategy

### **Supporting information.**

Additional SEM, XPS, Raman spectra and fitted curves with fitting details are provided in supplementary information.

### **Authors contributions**

S.G. planned and conceptualized the work, did the synthesis and characterizations of the materials, and wrote the manuscript. A.M., D.O. and A.M. assisted in PLD deposition. M.R. assisted in the electrochemical measurements and analysis. F.G. did the XPS measurements under the supervision of G.B.. V.R. helped in Raman spectroscopic analysis. D.D. and C.S.C. gave useful comments for the conceptualization of the work. All authors edited the manuscript and approved the final version of the manuscript.

### **Notes**

The authors declare no competing financial interest.

### **Acknowledgements**

S.G thank Horizon Europe (HORIZON) for the Marie Skłodowska-Curie Fellowship (grant no. 101067998-ENHANCER). Carlo S. Casari acknowledges partial funding from the European Research Council (ERC) under the European Union's Horizon 2020 Research and Innovation Program ERC Consolidator Grant (ERC CoG2016 EspLORE Grant Agreement 724610, website: [www.esplora.polimi.it](http://www.esplora.polimi.it)). Carlo S. Casari also acknowledges funding by the project funded under the National Recovery and Resilience Plan (NRRP), Mission 4 Component 2 Investment 1.3 Call for Tender 1561 of 11.10.2022 of Ministero dell'Università e della Ricerca (MUR), funded by the European Union NextGenerationEU Award Project Code PE0000021, Concession Decree 1561 of 11.10.2022 adopted by Ministero dell'Università e della Ricerca (MUR), CUP D43C22003090001, Project "Network 4 Energy Sustainable Transition (NEST)". We thank Alessandro Zani, former PhD student at NanoLab, POLIMI for the MATLAB program for fitting the Raman spectra by BWF function. We also thank Alberto Calloni for the useful discussion on XPS analysis.

### **Conflict of interests**

The authors declare no conflict of interest.

### **Data Availability statement**

All the data of this study are available in the main manuscript and the Supplementary Information.

## References:

- [1] I. Kim, C. Shim, S.W. Kim, C. Lee, J. Kwon, K. Byun, U. Jeong, Amorphous Carbon Films for Electronic Applications, *Adv. Mater.* 35 (2023). <https://doi.org/10.1002/adma.202204912>.
- [2] H. Mahajan, K.U. Mohanan, S. Cho, Facile Synthesis of Biocarbon-Based MoS<sub>2</sub> Composite for High-Performance Supercapacitor Application, *Nano Lett.* 22 (2022) 8161–8167. <https://doi.org/10.1021/acs.nanolett.2c02595>.
- [3] T. Lin, I.-W. Chen, F. Liu, C. Yang, H. Bi, F. Xu, F. Huang, Nitrogen-doped mesoporous carbon of extraordinary capacitance for electrochemical energy storage, *Science* (80-. ). 350 (2015) 1508–1513. <https://doi.org/10.1126/science.aab3798>.
- [4] C. Casari, A. Bassi, Pulsed Laser Deposition of Nanostructured Oxides for Emerging Applications, in: *Oxide Nanostructures*, Pan Stanford Publishing, 2014: pp. 99–114. <https://doi.org/10.1201/b15633-3>.
- [5] A.J. Haider, T. Alawsi, M.J. Haider, B.A. Taha, H.A. Marhoon, A comprehensive review on pulsed laser deposition technique to effective nanostructure production: trends and challenges, *Opt. Quantum Electron.* 54 (2022) 1–25. <https://doi.org/10.1007/s11082-022-03786-6>.
- [6] B. Bayatsarmadi, Y. Zheng, C.S. Casari, V. Russo, S.-Z. Qiao, Pulsed laser deposition of porous N-carbon supported cobalt (oxide) thin films for highly efficient oxygen evolution, *Chem. Commun.* 52 (2016) 11947–11950. <https://doi.org/10.1039/C6CC04776A>.
- [7] A. Maffini, A. Pazzaglia, D. Dellasega, V. Russo, M. Passoni, Correction to: Production of Carbon Nanofoam by Pulsed Laser Deposition on Flexible Substrates, in: 2022: pp. C1–C1. [https://doi.org/10.1007/978-3-030-81827-2\\_9](https://doi.org/10.1007/978-3-030-81827-2_9).
- [8] A. Hu, M. Rybachuk, Q.-B. Lu, W.W. Duley, Direct synthesis of sp-bonded carbon chains on graphite surface by femtosecond laser irradiation, *Appl. Phys. Lett.* 91 (2007) 131906. <https://doi.org/10.1063/1.2793628>.
- [9] N.A. Kyeremateng, T. Brousse, D. Pech, Microsupercapacitors as miniaturized energy-storage components for on-chip electronics, *Nat. Nanotechnol.* 12 (2017) 7–15. <https://doi.org/10.1038/nnano.2016.196>.
- [10] S. Ghosh, J. Wang, G. Tontini, S. Barg, Electrodes for Flexible Micro-Supercapacitors, *Flex. Supercapacitor Nanoarchitectonics.* (2021) 413–460. <https://doi.org/10.1002/9781119711469.ch14>.
- [11] S. Ghosh, S.R. Polaki, P.K. Ajikumar, N.G. Krishna, M. Kamruddin, Aging effects on vertical graphene nanosheets and their thermal stability, *Indian J. Phys.* 92 (2018) 337–342. <https://doi.org/10.1007/s12648-017-1113-0>.
- [12] S. Ghosh, S.K. Behera, A. Mishra, C.S. Casari, K.K. Ostrikov, Quantum Capacitance of Two-Dimensional-Material-Based Supercapacitor Electrodes, *Energy & Fuels.* 37 (2023) 17836–17862. <https://doi.org/10.1021/acs.energyfuels.3c02714>.
- [13] Z. Supiyeva, X. Pan, Q. Abbas, The critical role of nanostructured carbon pores in supercapacitors, *Curr. Opin. Electrochem.* 39 (2023) 101249. <https://doi.org/10.1016/j.coelec.2023.101249>.
- [14] M.K. Hoque, J.A. Behan, J. Creel, J.G. Lunney, T.S. Perova, P.E. Colavita, Reactive Plasma N-Doping of Amorphous Carbon Electrodes: Decoupling Disorder and Chemical Effects on Capacitive and Electrocatalytic Performance, *Front. Chem.* 8 (2020) 593932. <https://doi.org/10.3389/fchem.2020.593932>.
- [15] M. Ayiania, M. Smith, A.J.R. Hensley, L. Scudiero, J.-S. McEwen, M. Garcia-Perez,

- Deconvoluting the XPS spectra for nitrogen-doped chars: An analysis from first principles, *Carbon N. Y.* 162 (2020) 528–544. <https://doi.org/10.1016/j.carbon.2020.02.065>.
- [16] M. Smith, L. Scudiero, J. Espinal, J.-S. McEwen, M. Garcia-Perez, Improving the deconvolution and interpretation of XPS spectra from chars by ab initio calculations, *Carbon N. Y.* 110 (2016) 155–171. <https://doi.org/10.1016/j.carbon.2016.09.012>.
- [17] A. Ciszewski, B. Rydzyńska, Studies on self-assembly phenomena of hydrophilization of microporous polypropylene membrane by acetone aldol condensation products: New separator for high-power alkaline batteries, *J. Power Sources.* 166 (2007) 526–530. <https://doi.org/10.1016/j.jpowsour.2007.01.034>.
- [18] A. Pazzaglia, A. Maffini, D. Dellasega, A. Lamperti, M. Passoni, Reference-free evaluation of thin films mass thickness and composition through energy dispersive X-ray spectroscopy, *Mater. Charact.* 153 (2019) 92–102. <https://doi.org/10.1016/j.matchar.2019.04.030>.
- [19] S. Ghosh, K. Ganesan, S.R. Polaki, T.R. Ravindran, N.G. Krishna, M. Kamruddin, A.K. Tyagi, Evolution and defect analysis of vertical graphene nanosheets, *J. Raman Spectroscopy.* 45 (2014) 642–649. <https://doi.org/10.1002/jrs.4530>.
- [20] A. Barinov, O.B. Malcioğlu, S. Fabris, T. Sun, L. Gregoratti, M. Dalmiglio, M. Kiskinova, Initial Stages of Oxidation on Graphitic Surfaces: Photoemission Study and Density Functional Theory Calculations, *J. Phys. Chem. C.* 113 (2009) 9009–9013. <https://doi.org/10.1021/jp902051d>.
- [21] M. Pervolaraki, P. Komninou, J. Kioseoglou, A. Othonos, J. Giapintzakis, Ultrafast pulsed laser deposition of carbon nanostructures: Structural and optical characterization, *Appl. Surf. Sci.* 278 (2013) 101–105. <https://doi.org/10.1016/j.apsusc.2013.03.015>.
- [22] E. Mohagheghpour, M. Rajabi, R. Gholamipour, M.M. Larijani, S. Sheibani, Correlation study of structural, optical and electrical properties of amorphous carbon thin films prepared by ion beam sputtering deposition technique, *Appl. Surf. Sci.* 360 (2016) 52–58. <https://doi.org/10.1016/j.apsusc.2015.10.213>.
- [23] T. Danno, XPS Study of Carbyne-Like Carbon Films, in: *AIP Conf. Proc.*, AIP, 2004: pp. 431–434. <https://doi.org/10.1063/1.1812123>.
- [24] A.P. Piedade, L. Canguero, Influence of Carbyne Content on the Mechanical Performance of Nanothick Amorphous Carbon Coatings, *Nanomaterials.* 10 (2020) 780. <https://doi.org/10.3390/nano10040780>.
- [25] S.I. Moseenkov, V.L. Kuznetsov, N.A. Zolotarev, B.A. Kolesov, I.P. Prosvirin, A. V. Ishchenko, A. V. Zavorin, Investigation of Amorphous Carbon in Nanostructured Carbon Materials (A Comparative Study by TEM, XPS, Raman Spectroscopy and XRD), *Materials (Basel).* 16 (2023) 1112. <https://doi.org/10.3390/ma16031112>.
- [26] C.S. Casari, C.S. Giannuzzi, V. Russo, Carbon-atom wires produced by nanosecond pulsed laser deposition in a background gas, *Carbon N. Y.* 104 (2016) 190–195. <https://doi.org/10.1016/j.carbon.2016.03.056>.
- [27] G. Sahoo, S.R. Polaki, S. Ghosh, N.G. Krishna, M. Kamruddin, K. (Ken) Ostrikov, Plasma-tunable oxygen functionalization of vertical graphenes enhance electrochemical capacitor performance, *Energy Storage Mater.* 14 (2018) 297–305. <https://doi.org/10.1016/j.ensm.2018.05.011>.
- [28] C. Casiraghi, A.C. Ferrari, J. Robertson, Raman spectroscopy of hydrogenated amorphous carbons, *Phys. Rev. B.* 72 (2005) 085401. <https://doi.org/10.1103/PhysRevB.72.085401>.
- [29] A.C. Ferrari, S.E. Rodil, J. Robertson, Interpretation of infrared and Raman spectra of amorphous carbon nitrides, *Phys. Rev. B.* 67 (2003) 155306.

<https://doi.org/10.1103/PhysRevB.67.155306>.

- [30] A. Maffini, A. Pazzaglia, D. Dellasega, V. Russo, M. Passoni, Growth dynamics of pulsed laser deposited nanofoams, *Phys. Rev. Mater.* 3 (2019) 1–9. <https://doi.org/10.1103/PhysRevMaterials.3.083404>.
- [31] S. Ghosh, S. Barg, S.M. Jeong, K.K. Ostrikov, Heteroatom-Doped and Oxygen-Functionalized Nanocarbons for High-Performance Supercapacitors, *Adv. Energy Mater.* 10 (2020) 2001239. <https://doi.org/10.1002/aenm.202001239>.
- [32] N. Frese, S. Taylor Mitchell, C. Neumann, A. Bowers, A. Götzhäuser, K. Sattler, Fundamental properties of high-quality carbon nanofoam: from low to high density, *Beilstein J. Nanotechnol.* 7 (2016) 2065–2073. <https://doi.org/10.3762/bjnano.7.197>.
- [33] Z.G. Neale, M.J. Lefler, J.W. Long, D.R. Rolison, M.B. Sassin, R. Carter, Freestanding carbon nanofoam papers with tunable porosity as lithium–sulfur battery cathodes, *Nanoscale.* 15 (2023) 16924–16932. <https://doi.org/10.1039/D3NR02699J>.
- [34] Z. Li, S. Gao, H. Mi, C. Lei, C. Ji, Z. Xie, C. Yu, J. Qiu, High-energy quasi-solid-state supercapacitors enabled by carbon nanofoam from biowaste and high-voltage inorganic gel electrolyte, *Carbon N. Y.* 149 (2019) 273–280. <https://doi.org/10.1016/j.carbon.2019.04.056>.
- [35] S. Nufer, P. Lynch, M. Cann, M.J. Large, J.P. Salvage, S. Víctor-Román, J. Hernández-Ferrer, A.M. Benito, W.K. Maser, A. Brunton, A.B. Dalton, Carbon Nanofoam Supercapacitor Electrodes with Enhanced Performance Using a Water-Transfer Process, *ACS Omega.* 3 (2018) 15134–15139. <https://doi.org/10.1021/acsomega.8b02118>.
- [36] N. Muchlisha, D.M. Widjonarko, T.E. Saraswati, Synthesis of drug carrier carbon nanofoam by chemical vapor deposition using Agar/NaCl catalyst, *J. Phys. Conf. Ser.* 2556 (2023) 012006. <https://doi.org/10.1088/1742-6596/2556/1/012006>.
- [37] J. Xue, Z. Gao, L. Xiao, T. Zuo, J. Gao, D. Li, L. Qu, An Ultrafast Supercapacitor Based on 3D Ordered Porous Graphene Film with AC Line Filtering Performance, *ACS Appl. Energy Mater.* 3 (2020) 5182–5189. <https://doi.org/10.1021/acsaem.9b02458>.
- [38] N. Islam, J. Warzywoda, Z. Fan, Edge-Oriented Graphene on Carbon Nanofiber for High-Frequency Supercapacitors, *Nano-Micro Lett.* 10 (2018) 9. <https://doi.org/10.1007/s40820-017-0162-4>.
- [39] Z. Zhang, Z. Wang, F. Wang, T. Qin, H. Zhu, P. Liu, G. Zhao, X. Wang, F. Kang, L. Wang, C. Yang, A Laser-Processed Carbon-Titanium Carbide Heterostructure Electrode for High-Frequency Micro-Supercapacitors, *Small.* 19 (2023) 2300747. <https://doi.org/10.1002/smll.202300747>.
- [40] J.R. Miller, R.A. Outlaw, B.C. Holloway, Graphene Double-Layer Capacitor with ac Line-Filtering Performance, *Science* (80-. ). 329 (2010) 1637–1639. <https://doi.org/10.1126/science.1194372>.
- [41] Y. Rangom, X. (Shirley) Tang, L.F. Nazar, Carbon Nanotube-Based Supercapacitors with Excellent ac Line Filtering and Rate Capability via Improved Interfacial Impedance, *ACS Nano.* 9 (2015) 7248–7255. <https://doi.org/10.1021/acsnano.5b02075>.
- [42] Y.J. Kang, Y. Yoo, W. Kim, 3-V Solid-State Flexible Supercapacitors with Ionic-Liquid-Based Polymer Gel Electrolyte for AC Line Filtering, *ACS Appl. Mater. Interfaces.* 8 (2016) 13909–13917. <https://doi.org/10.1021/acsaami.6b02690>.
- [43] V.K. Mariappan, K. Krishnamoorthy, S. Manoharan, P. Pazhamalai, S. Kim, Electrospun Polymer-Derived Carbyne Supercapacitor for Alternating Current Line Filtering, *Small.* 17 (2021) 2102971. <https://doi.org/10.1002/smll.202102971>.
- [44] Z.J. Han, C. Huang, S.S. Meysami, D. Piche, D.H. Seo, S. Pineda, A.T. Murdock, P.S. Bruce, P.S.

Grant, N. Grobert, High-frequency supercapacitors based on doped carbon nanostructures, Carbon N. Y. 126 (2018) 305–312. <https://doi.org/10.1016/j.carbon.2017.10.014>.



## SUPPLEMENTARY INFORMATION

### Ballistic-aggregated Amorphous Carbon Nanofoam in Target side of Pulsed Laser Deposition for Energy Storage Applications

Subrata Ghosh<sup>1\*</sup>, Massimiliano Righi<sup>1</sup>, Andrea Macrelli<sup>1</sup>, Davide Orecchia, Alessandro Maffini<sup>1</sup>, Francesco Goto<sup>2</sup>, Gianlorenzo Bussetti<sup>2</sup>, David Dellasega<sup>1</sup>, Valeria Russo<sup>1</sup>, Andrea Li Bassi<sup>1</sup>, Carlo S. Casari<sup>1\*</sup>

<sup>1</sup> *Micro and Nanostructured Materials Laboratory – NanoLab, Department of Energy, Politecnico di Milano, via Ponzio 34/3, Milano, 20133, Italy*

<sup>2</sup> *Solid Liquid Interface Nano-Microscopy and Spectroscopy (SoLINano- $\Sigma$ ) lab, Department of Physics, Politecnico di Milano, Piazza Leonardo da Vinci 32, 20133 Milano, Italy*

Corresponding author email: [subrata.ghosh@polimi.it](mailto:subrata.ghosh@polimi.it) (S.G.) and [carlo.casari@polimi.it](mailto:carlo.casari@polimi.it) (C.S.C.)

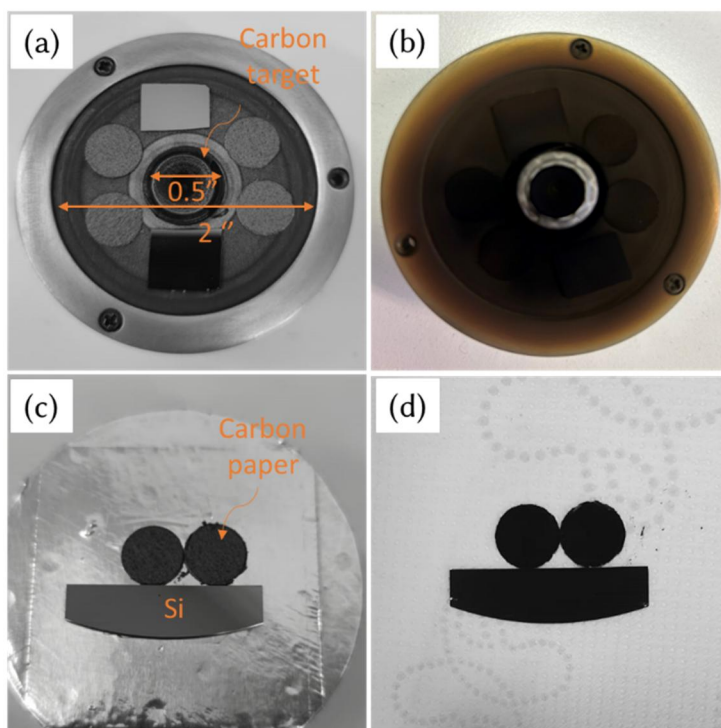


**Figure S1:** Photograph of target holder (a) before and (b) after carbon nanofoam deposition. Photograph of (a) substrate holder with the substrate before deposition and (b) substrate after deposition.

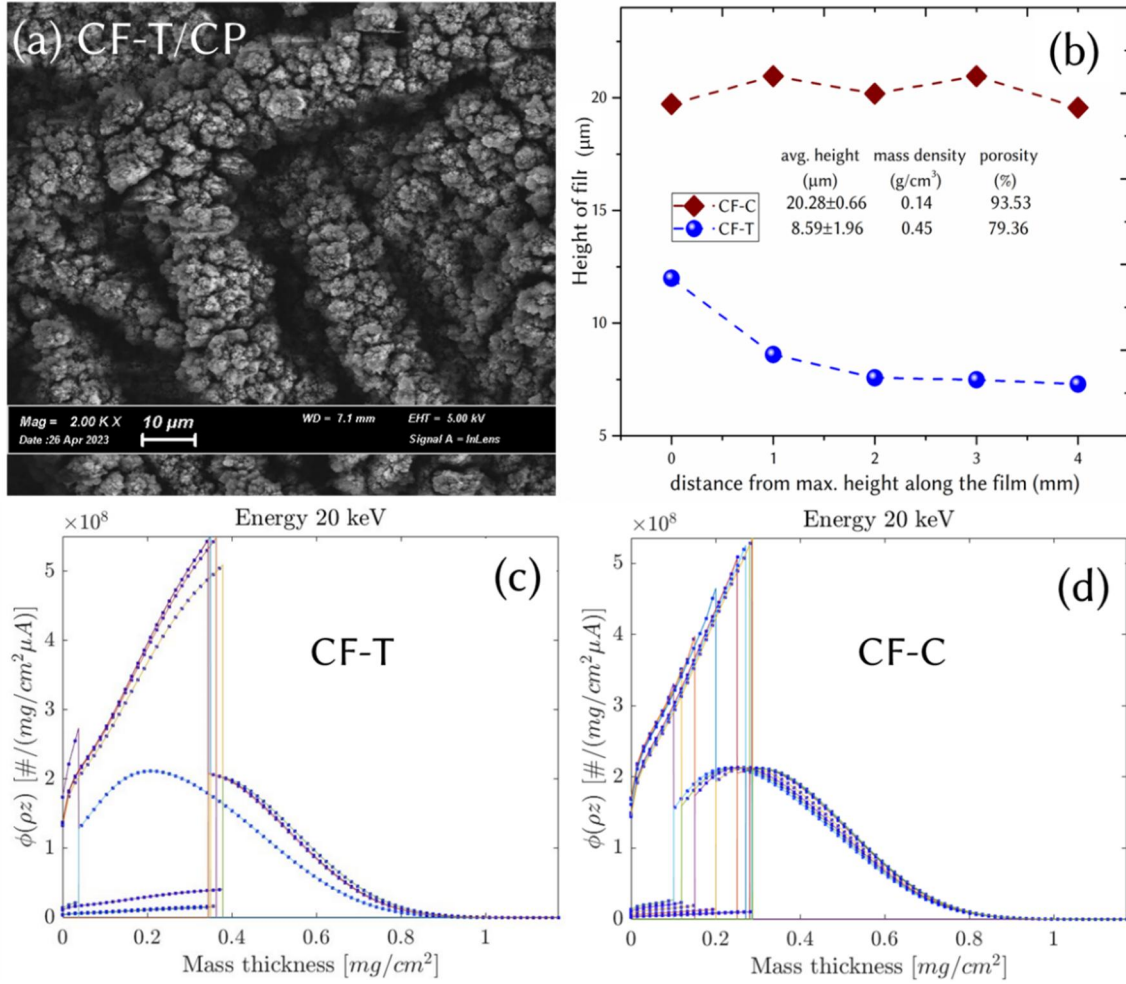


**Figure S2:** (a) scanning electron micrograph of CF-T grown on carbon paper, CP. (b) plot of height of the CF-T and CF-C film. Quantified average height, mass density and porosity of the films are provided in the inset of plot. (b) Simulated data of mass-density calculation of carbon nanofoam (c) CF-T and (d) CF-C using EDDIE software. The y-axis of plot (c-d) represent X-ray generation distribution function ( $\phi(\rho z)$ ) in samples and each colored line corresponds to the iteration.

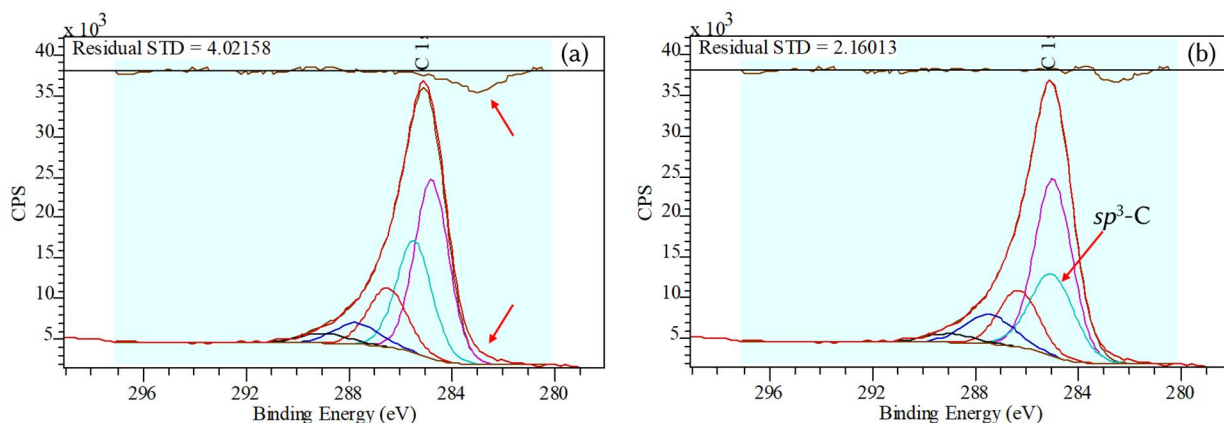


**Figure S3:** Casa XPS fitted C1s spectra without considering the peak  $sp$ -C at binding energy at around 283.8 eV. (a) Deconvoluted C1s spectra without  $sp$ -C peak shows higher residual STD of 4.02158. (b) fitted C1s spectra with deconvoluted peaks and without  $sp$ -C. In this fit, one peak ( $sp^3$ -C peak – sky blue color) lies under another peak ( $sp^2$ -C peak - pink colour). This fitting is not scientifically reliable. In the figure CPS stand for count per second and STD stand for standard deviation.

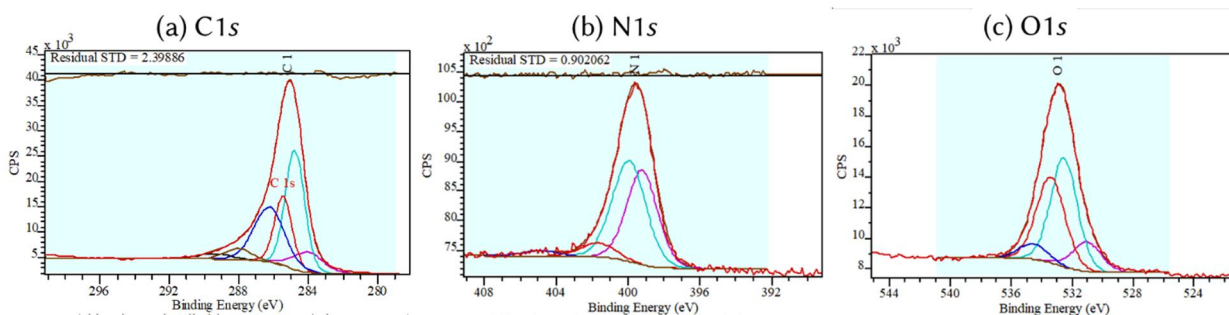


**Figure S4.** Casa XPS fitted High resolution (a) C1s, (b) N1s and (c) O1s spectra with deconvoluted peaks of CF-C.

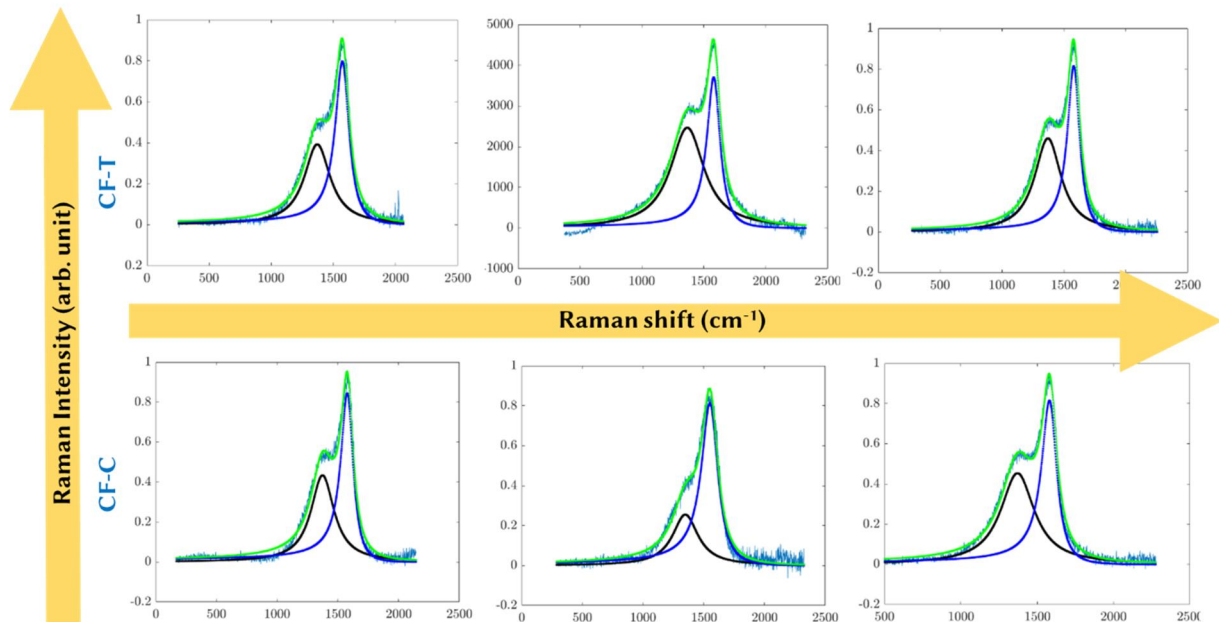


Figure S5: Fitted 1<sup>st</sup>-order Raman spectra of (top panel) CF-T and (bottom panel) CF-C taken at different position/samples using the MATLAB program. D-peak is Lorentzian shape and G-peak is fitted with BWF-lineshape

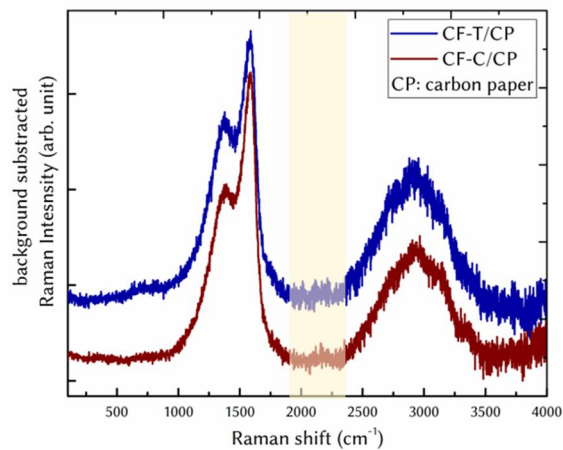


Figure S6: Raman spectra of CF-T and CF-C on carbon paper. A very weak *sp*-band is also observed for the sample on carbon paper, which is marked by highlighting region along with the other prominent peaks.

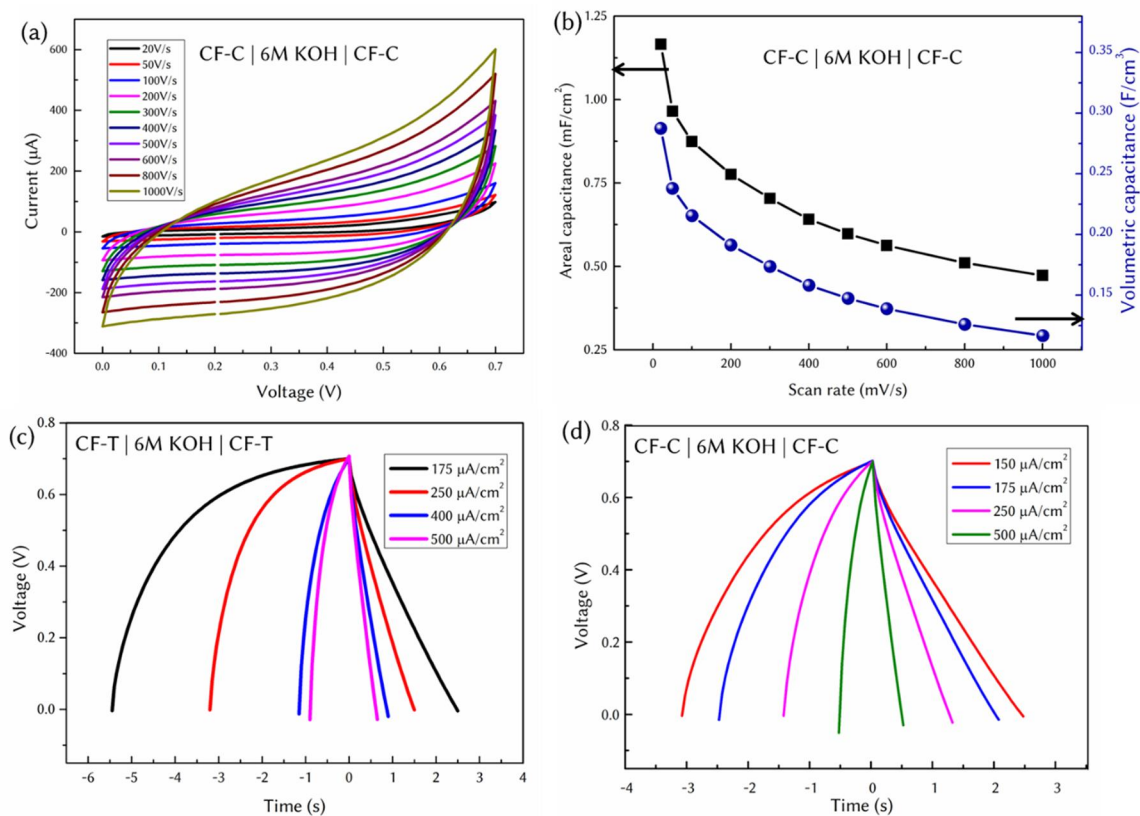


Figure S7: Electrochemical performance of symmetric device. (a) cyclic voltammogram profile and (b) areal and volumetric capacitance at different scan rate of CF-C1. Current density dependent Charge-discharge profile of (c) CF-T and (d) CF-C device.

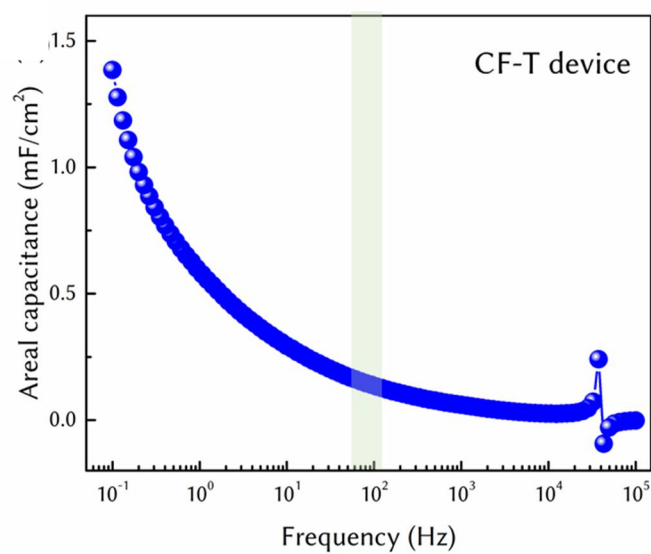
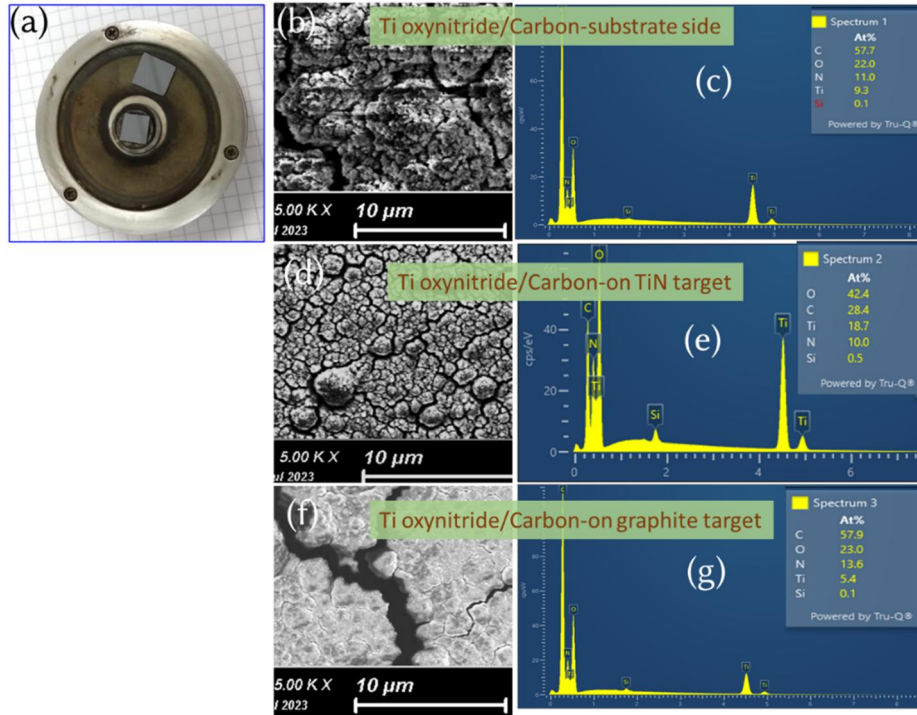


Figure S8: Frequency-dependent areal capacitance CF-T device.



**Figure S9:** (a) Optical micrograph of the target side, where Si substrate is placed on graphite target and TiN target. Scanning electron micrograph and corresponding EDX spectra of oxynitride/carbon composite prepared on the (b-c) substrate-side, (d-e) on TiN in target side and (f-g) on graphite in target side.